CIRP Annals - Manufacturing Technology 69 (2020) 441–444

Contents lists available at ScienceDirect

CIRP Annals - Manufacturing Technology

journal homepage: https://www.editorialmanager.com/CIRP/default.aspx

In-situ calibration of laser/galvo scanning system using dimensional reference artefacts

H. Yeung, B.M. Lane, M.A. Donmez (2)*, S. Moylan

Engineering Laboratory, National Institute of Standards and Technology, Gaithersburg, MD 20899, United States

ARTICLE INFO

Article history:
Available online 17 May 2020

Keywords:
Selective laser melting (SLM)
Positioning
Galvo Calibration

ABSTRACT

Laser powder bed fusion systems use a high-power laser, steered by two galvanometer (galvo) mirrors to scan a pattern on metal powder layers. Part geometric tolerances depend on the positioning accuracy of the laser/galvo system. This paper describes an in-situ calibration technique utilizing a camera coaxially aligned with the laser imaging a dimensional reference artefact. The laser positions are determined from the images captured by the camera while scanning the artefact. The measurement uncertainty is estimated using simulations. The in-situ calibration results are compared with the results obtained from the typical 'mark and measure' galvo calibration method.

Published by Elsevier Ltd on behalf of CIRP.

1. Introduction

An important component pertaining to geometric accuracy of a laser powder bed fusion (LPBF) system is the galvanometer (galvo) mirrors, which steer a focused laser beam along prescribed geometric patterns on the powder bed, forming each layer of the printed part. These galvo systems require geometric calibration, establishing that the commanded laser positions match the specified positions on the build plane. The traditional 'mark and measure' calibration method requires a grid or a pattern to be inscribed on a substrate, which can be coated glass [1], anodized metal plate [2], or laser burn paper, then the geometric accuracy of that pattern is evaluated via ex-situ measurement on an optical coordinate measuring machine (CMM). The main limitations of this method are the influence of the inscribing (burning) process in patterning and the lack of direct correlation between the commanded position and the measured position on the pattern.

In this paper, we describe a new galvo calibration method that uses the same hardware as a coaxial melt pool imaging system, similar to those widely used for LPBF process monitoring research [3], and found on many commercial LPBF machines [4]. This method incorporates an in-situ reference scale based on a calibrated artefact and an illumination source and can be rapidly executed, with a potential for complete automation.

2. Calibration method

The calibration method utilizes a camera coaxially aligned with the processing laser, capturing images of a dimensional reference artefact (optical target) while scanning it with the galvo system following a programmed path. Fig. 1a shows the coaxial imaging setup. Fig. 1b shows a typical optical target, and the three coordinate systems defined by target (T), galvo (G), and camera (C), respectively. All captured image positions are originally in camera coordinates (C) and denoted by ${}^{C}\mathbf{p}$. All scan command positions are in G and denoted by ${}^{G}\mathbf{p}_{cmd}$. To compare these two sets of positions, image positions in camera coordinate system are transferred to galvo coordinate system by first a nonlinear transformation, ${}^{T}H_{C}$, between camera and target coordinate systems, and then a rotational transformation, ${}^{G}H_{T}$, between target and galvo coordinate systems as shown in Eq. (1).

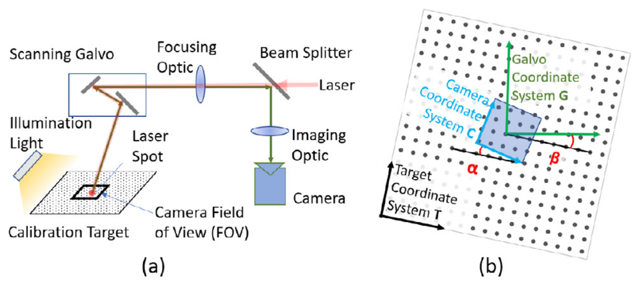

Fig. 1. (a) Schematic of coaxial imaging of an optical target, with equally-spaced markers, on an LPBF system. (b) Galvo, optical target, and camera coordinate systems.

$$ {}^{G}\mathbf{p}={}^{G}H_{T}\cdot{}^{T}H_{C}\cdot{}^{C}\mathbf{p} \quad (1)$$

Descriptions of the coordinate transformations are given later in this section. For calibration purposes, the measured position error ${}^{G}\mathbf{e}$, in galvo coordinate system G, can then be obtained by Eq. (2).

$$ {}^{G}\mathbf{p}={}^{G}\mathbf{p}_{cmd}-{}^{C}\mathbf{p} \quad (2)$$

Official contribution of the National Institute of Standards and Technology; not subject to copyright in the United States.

* Corresponding author.
E-mail address: alkan.donmez@nist.gov (M.A. Donmez).

https://doi.org/10.1016/j.cirp.2020.03.016
0007-8506/Published by Elsevier Ltd on behalf of CIRP.

Since the processing laser and the camera point to the same location through the same optical path, the laser spot will always appear at the same position in the coaxial camera field of view (FOV) with a constant offset from the image center. Therefore, the laser/galvo position can be measured by finding the image center position within the target coordinate system. Theoretically, the image position may be found by pattern matching a unique feature on the target. But, most commercial, calibrated optical targets have equally-spaced, repeated markers, where an image can match to many locations on the target. So, a new approach based on the interframe displacement vector between sequential pairs of image frames is developed for this purpose.

2.1. Interframe displacement vector

If the camera FOV is moved by the scanning galvo over an optical target, an image frame sequence similar to Fig. 2 will be captured. FOV and scan step size are selected to ensure at least one complete marker is in the FOV at all times and no neighbouring marker is skipped. In each frame, a marker is identified as the 'tracer' by image cross-correlation described later. If the same marker is identified in two consecutive image frames j and j-1, such as marker 1 in frames 1–5 in Fig. 2, the interframe displacement vector (Δx_j, Δy_j) of frame j can be found by Eq. (3), where ($x_{i,j}$, $y_{i,j}$) is the coordinates of the tracer marker i in frame j.

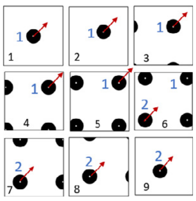

Fig. 2. Simulated coaxial image frame sequences. Galvo moves to the opposite direction of the red arrows. (For interpretation of the references to colour in this figure legend, the reader is referred to the web version of this article.)

$$\Delta x_j = x_{i,j} - -x_{i,j\text{-}1;} \Delta y_j = y_{i,j} - -y_{i,j\text{-}1} \tag{3}$$

When a different marker is identified as the tracer, such as marker 2 appearing in frame 6, the distance between these two tracers needs to be accounted for by Eq. (4).

$$\begin{aligned}\Delta x_j &= \left(x_{i,j} - x_{i\text{-}1,j\text{-}1}\right) + \left(x_{i\text{-}1,j} - x_{i,j}\right)\\ \Delta y_j &= \left(y_{i,j} - y_{i\text{-}1,j\text{-}1}\right) + \left(y_{i\text{-}1,j} - y_{i,j}\right)\end{aligned} \tag{4}$$

The vector distance between these two tracers can be determined by Eq. (5).

$$x_{i\text{-}1,j} - -x_{i,j} = d \cdot \cos\theta; y_{i\text{-}1,j} - -y_{i,j} = d \cdot \sin\theta \tag{5}$$

where d can be s or $\sqrt{2}$s, and s is the calibrated distance between adjacent markers. Assuming the scan path is perfectly aligned with the target, θ can be 0, 45, or 90° depending on if they are horizontal, vertical or diagonal neighbours. In more generic form, Eq. (3) can be considered as a special case with $d = 0$ (same tracer). Displacement vector (Δx_j, Δy_j) is calculated with each of the four pairs of the (d, θ) values: (0, 0), (s, 0), (s, 90) and ($\sqrt{2}$s, 45), and the one that gives a value closest to the commanded step size is chosen. Thus, the interframe displacement vectors between all consecutive frames can be determined and the complete measured scan path can be reconstructed by summing all these vectors and compared against the commanded scan path. Fig. 3 shows an example of a scan path reconstruction from 7870 image frames. This approach is like a two-dimensional incremental optical encoder using the camera as an optical sensor and image analysis to determine the incremental displacement. The locations of the markers in the image frame are determined by image cross-correlation [5]. In signal processing, cross-correlation is used for detecting a known feature (pattern) within a larger data set (a template). In digital image processing, functions f and t represent the gray intensity of the pattern and template images at pixel (x, y). For these functions the cross-correlation is defined in Eq. (6), where u and v represent translation of images with step size of 1 pixel. $R(u, v)$ is maximized when a subimage in t, with same size as f and center at (u, v), best matches with f. As pixel coordinate is discrete, (u, v) are integers. A subpixel resolution can be achieved by interpolating the 3-pixel x 3-pixel area surrounding (u, v).

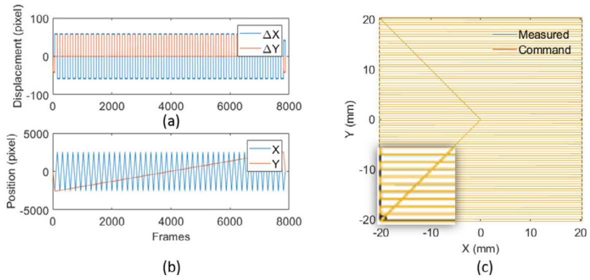

Fig. 3. Scan path reconstruction. (a) Interframe displacement vector Δx and Δy. (b) Displacement $x = \sum\Delta$x and $y = \sum\Delta$y. (c) Measured path superimposed with command path. The lower left corner is an enlarged view. (For interpretation of the references to colour in this figure legend, the reader is referred to the web version of this article.)

$$R(u, v) = \sum_{x,y} f(x, y)t(x - u,\ y - v) \tag{6}$$

To determine the locations of the markers in the image, the image of the marker is used as the pattern (f) and the full image as the template (t). The correlation coefficient R is plotted in Fig. 4a. The peak indicates where the greatest similarities are found. Fig. 4b marks the locations of the peaks for each test image (see Fig. 2) by red 'x', which overlap with the centers of the markers identified as tracers. Multiple markers can be identified in the same image by searching for the next correlation peak.

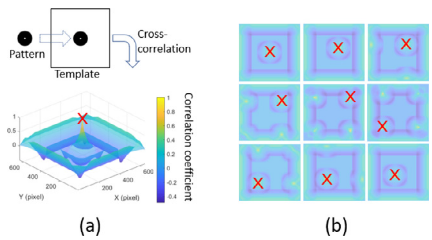

Fig. 4. Detect marker position in coaxial images. (a) Normalized correlation coefficients. (b) Cross-correlation of marker pattern and coaxial images.

2.2. Image alignment

Various optical components of the system shown in Fig. 1, as well as imperfect camera alignment with the optical target can distort camera images. As a result, equally spaced markers on the optical target may not appear equally spaced in the images. This distortion must be corrected by image alignment before the images are used for position measurement. Image alignment is achieved by a nonlinear transformation, $^{T}H_{C}$, between the captured image and the known target marker spacing [6]. A mapping is first created between the marker positions in the image and their true positions on the target, and a 3rd order polynomial is fitted to transform the image to target coordinate system. To ensure a robust fitting, the number of markers in both sets should be as large as possible. Therefore, we use intermediate mini markers in the shape of '+', which are available in most optical targets, between the main markers (circles).

In summary, there are seven major steps for this calibration method: (1) Select a dimensional reference artefact and camera with appropriate FOV. (2) Design a scan path and step size to dwell at each step along the path to trigger the camera. (3) Scan the target and take images at each dwell position. (4) Align the images (transform positions) to the target coordinate system. (5) Determine the interframe displacement vectors and construct the measured path in the target coordinate system. (6) Transform the measured path to the galvo coordinate system by a rotation of β, which can be easily determined if part of the command path is planned in the x-direction only. This rotation is the ${}^{G}H_T$ in Eq. (1). Only one galvo axis should be used for alignment, as the galvos may not be perfectly orthogonal or equally scaled. (7) Compare the measured path with the commanded path to obtain galvo position error. Once the galvo is calibrated, the origin of galvo coordinate system is established by the processing laser projecting in the normal direction to the build plane. Since any error between the measured position and the actual position will directly affect the calibration results, it is analysed in next section.

3. Measurement uncertainty analysis

The main uncertainty components of the image-based measurement method fall into two categories: image processing and image alignment (by curve fitting). The uncertainty analysis is conducted based on simulated images created by cropping rectangular regions, representing the camera FOV, out of a high-resolution bitmap image representing the whole optical target. These simulated images are then processed with the method described in the previous section to obtain the 'measured' positions. The central locations of cropped images are the 'actual' positions. The differences between measured and actual positions are directly related to the measurement uncertainty.

3.1. Cross-correlation induced errors

An image sequence is created by simulating a scan over a simulated optical target, which is a bitmap of 8 µm per pixel resolution with 17 rows and 17 columns of circles of 1 mm diameter spaced 3 mm apart. The scan path is designed to cover an area of a 40.6 mm x 40.6 mm square with 88 dwell (sampling) positions along each direction (of the 88 × 88 grid). The interval between two adjacent sampling positions is 40.6/87 ≈ 0.467 mm and is referred to as step size. The same dwell position intervals (step sizes) are programmed along orthogonal and diagonal paths. Images are 'taken' by cropping a frame of 520 pixels x 520 pixels from the optical target centered at the dwell positions. A total of 7870 image frames are sampled along the scan path. A sequence of images is hence created such as shown in Fig. 2 and is referred to as 'ideal' images. This is equivalent to imaging an optical target through a coaxial camera in ideal conditions, where the target, galvo, and camera are perfectly aligned, and there are no lens/mirror distortions of any kind. The interframe vectors obtained from the images by the cross-correlation and the resulting reconstructed path are shown in Fig. 3. Comparing this reconstructed path with the commanded positions, the average error is found to be less than 0.04 µm with a standard deviation (σ) less than 0.87 µm along both x- and y-directions.

3.2. Image alignment induced errors

Due to misalignments between camera and the galvo scanner optical path mentioned earlier, the images from actual calibration will be rotated and distorted compared to ideal images. To simulate this, a set of ideal images are first rotated by 10°, and then distorted by polynomials $x_2 = 0.995 \times_1 + 0.01y_1$ and $y_2 = -0.005 \times_1 + 0.997y_1$, where (x_1, y_1) is the location of the pixel on the original image, and (x_2, y_2) is its location on the distorted image. A sample distorted image consisting of main and intermediate markers is shown in Fig. 5a, indicating

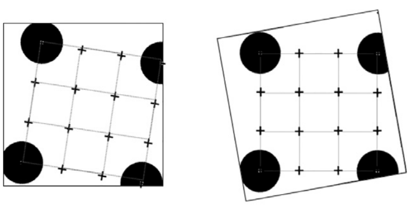

(a) (b)

Fig. 5. Image alignment example. (a) Distorted image, where markers do not fall into the 3 mm x 3 mm grid. (b) Aligned image by third-order polynomials.

deviations from their ideal grid locations. The distortion used here is a simple example. The actual distortion can be more complicated, but the same image restoration method can be applied as it assumes no information about the distortion.

The locations of these 4 × 4 markers on the distorted image are manually identified and mapped to the 4 × 4 grid nodes according to their true target positions. A 3rd-order polynomial in the form of Eq. (7) (shows only x component of transformation) is fit onto this mapping and used to transform all the pixels in the image. Aligned image is shown in Fig. 5b, where all markers fall on the same pixels of the grid nodes. Such aligned images are then processed as ideal images for inter-frame vector determination and path reconstruction.

$$x_1 = a_1 + a_2x_2 + a_3y_2 + a_4x_2\ y_2 + a_5x_2^2 + a_6y_2^2 + a_7x_2^2y_2 + a_8x_2y_2^2 + a_9x_2^3 + a_{10}y_2^3 \quad (7)$$

Comparing the reconstructed path with the command positions, the average error is found to be 7.31 µm with a σ of 5.32 µm in x-direction, and 5.25 µm with a σ of 2.41 µm in y-direction. At the resolution of 8 µm per 1 pixel, the average error is less than 1 pixel. The larger error for image alignment may come from discrete pixelization and from manual identification of the marker position. If needed, more complicated lens distortion models can be used to reduce uncertainty associated with this fitting transformation [6]. The uncertainty analysis above is based on simulated images. The processing of actual images is also affected by resolution of the images, image contrast, and size/shape of the target pattern. These feed into the distortion correction and cross-correlation operations, and associated uncertainty. Since the camera resolution is relatively finer than the marker size, location of the detected peaks are likely sub-pixel resolution. The uncertainty associated with the calibration of optical target (from the vendor specifications) can be combined with above mentioned sources of uncertainty to reach final uncertainty assessment of the method.

The same alignment transformation function is used over the whole galvo scan range of motion. This assumes the distortion is location-independent, though this may not be the case. The laser beam, for example, may reflect off galvo mirrors with imperfect flatness at different locations. Ideally an alignment polynomial should be generated and applied to each individual image to compensate these variations. To automate this process, the locations of the 4 × 4 markers can be determined by image cross-correlation method.

4. Experimentation

A commercial target is used for this experiment, consisting of 289 feature groups in a grid of 17 row by 17 column (Fig. 6a). Each group has four concentric circle and five crosshair features of varying sizes, arranged in a 3 mm x 3 mm pattern (Fig. 6b). The A1 features (Fig. 6b) are used for the image cross-correlation. Starting from the bottom left corner (Fig. 6a), the scan path rasters horizontally and up in 0.467 mm steps. The scan is programmed to dwell at each step for 10 ms, the camera is triggered 1 ms after the scan stops, and camera exposure time is set to 8 ms, ensuring that images are taken only when the galvo is stationary. A total of 7870 images or measured positions are taken.

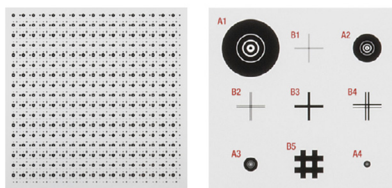

(a) (b)

Fig. 6. Commercial optical target. (a) Entire target consists of 289 feature groups of 3 mm x 3 mm each. (b) Close up of a group, where feature A1 is used as the marker for position detection.

Perfect alignment of the galvo coordinates and the target is not required. The FOV was chosen to be 520 pixels pixels x 520 pixels, or 4.16 mm x 4.16 mm at 8 μm/pixel resolution. The image window size is larger than the 3 mm x 3 mm target grid dimension, hence is guaranteed to at least one A1 feature appear in every image. The step size ensures a minimum of 7 images are taken per target pattern, regardless of scan path direction. The same parameters were used to create the simulation images in Section 2.

The experiment was conducted on a custom AM testbed [7] equipped with the scanning and imaging capabilities described above. Fig. 7a shows a sample image from the experiment, exhibiting rotation and distortion. The image is aligned per the same technique described in Section 2.2. The aligned image is shown in Fig. 7b. A 4×4 grid of 125 pixels spacing fits precisely on the 16 patterns of the aligned image, indicating a nearly 'ideal' image (matches the feature group grid in Fig. 6b) ready for path reconstruction. The scan path is reconstructed as described in Fig. 3. The differences between the measured and commanded positions are represented by the heat maps in Fig. 8. Note that the total error in Fig. 8 is an order of magnitude greater than the estimated measurement uncertainty provided in Section 3.

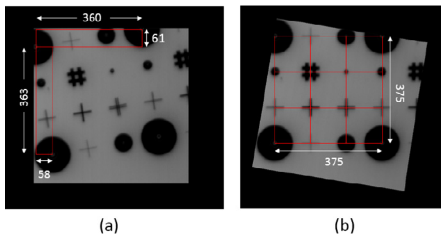

Fig. 7. Image alignment. (a) Raw image taken by coaxial camera. (b) Aligned image, centers of the patterns fall on the 4×4 grid node spacing at 125 pixels. Units are in pixels at 8 μm/pixel.

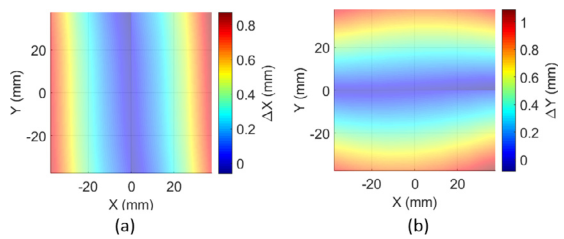

Fig. 8. Galvo position error detected by coaxial imaging method at 7870 imaging positions. (a) Error in x-direction. (b) Error in y-direction.

5. Summary and discussion

The galvo positioning error on the same AM testbed was also measured by the traditional 'mark and measure' approach. A pattern of 49 circular features with 0.5 mm diameter each was burned on a flat metal substrate with the laser, and subsequently measured ex-situ in an optical CMM. The position error vectors from both measurements are plotted in Fig. 9b. It shows the position error vectors from the two measurements tend to point in the same direction, have similar magnitudes, indicating similarity in the two measurement methods. However, direct comparison requires quantification of measurement uncertainty of the mark and measure method, which is outside the scope of this paper.

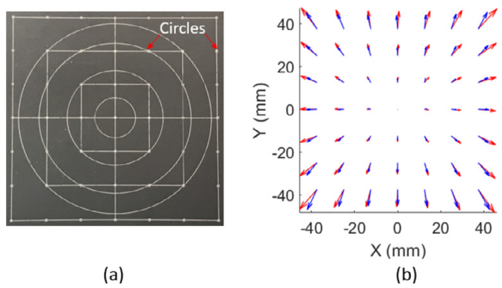

Fig. 9. (a) Mark and measure pattern. Centers of the 49 circles were measured by CMM. (b) Position error measured by 'mark and measure' (blue) and coaxial imaging (red) methods, arrows are 1:10 in scale. (For interpretation of the references to colour in this figure legend, the reader is referred to the web version of this article.)

Hence, it is demonstrated that the new in-situ method can effectively replace the traditional method. Users may prefer the new in-situ method for increased measurement densities or increased automation of calibration for more frequent compensation and accuracy improvements in existing systems. With a high-speed camera, the in-situ method can also be applied to measure the effect of dynamic galvo positioning errors. It can also be conducted immediately before builds, and applied in real-time to compensate for the galvo error to build more accurate parts.

References

[1] Land WS (2014) Effective Calibration and Implementation of Galvanometer Scanners as Applied to Direct Metal Laser Sintering. In: In: Proceedings of the ASPE 2014 Spring Topical Meeting *ASPE 2014 Spring Topical Meeting: Dimensional Accuracy and Surface Finish in Additive Manufacturing*, Berkeley, CA. American Society for Precision Engineering, pp 151–156.
[2] Lu Y (2017) *Error Characterization of EOS M280 Additive Manufacturing Machine* M.S. Thesis. Pennsylvania State University.
[3] Grasso M, Colosimo BM (2017) Process defects and in situ monitoring methods in metal powder bed fusion: a review. *Measurement Science and Technology* 28:044005.
[4] Kolb T, Elahi R, Seeger J, Soris M, Scheitler C, Hentschel O, Tremel J, Schmidt M (2019) Camera signal dependencies within coaxial melt pool monitoring in laser powder bed fusion. *Rapid Prototyping Journal*. in print.
[5] Lewis JP (1995) Fast Template Matching. *Vision Interface* : 120–123.
[6] Szeliski R (2005) *Handbook of Mathematical Models in Computer Vision*, Springer, 273–292.
[7] Yeung H, Lane BM, Donmez MA, Fox JC, Neira J (2018) Implementation of Advanced Laser Control Strategies for Powder Bed Fusion Systems. *Procedia Manufacturing* 26:871–879.